Improved Performance of Direct-Drive ICF Target Designs with Adiabat Shaping Using an Intensity Picket

Introduction

Hydrodynamic instabilities put severe constraints on target designs for inertial confinement fusion (ICF) experiments.[1,2] A large number of papers published over the last 30 years have been dedicated to the study of the seeding and subsequent growth of the hydrodynamic instabilities that develop during the shell implosion.[3] A particularly large effort (both theoretical and experimental) has been directed to understanding the growth rate of the dominant hydrodynamic instability—the Rayleigh–Taylor (RT) instability.[4] The RT instability inevitably occurs in systems where the heavier fluid is accelerated by the lighter fluid. Such conditions arise during the shell compression in ICF implosions, where the heavier shell material is accelerated by the lighter blowoff plasma.[1] The RT-instability growth amplifies the shell distortions seeded by initial surface roughness and laser nonuniformities (laser "imprint"). Grown to substantial amplitudes, the shell nonuniformities reduce the shell ρR and the neutron yield. Fortunately for ICF implosions, the thermal conduction that drives the ablation process creates several stabilizing effects that reduce both the nonuniformity seeding and the RT-growth rates.[3] Indeed, seeding due to the laser nonuniformity is determined by how quickly the plasma atmosphere is created around the imploding shell. The laser radiation is absorbed at some distance from the cold shell. The larger this distance (the conduction zone), the larger the smoothing effect[5] of the thermal conductivity within the conduction zone and the smaller the laser imprint. The stabilization of the RT modes is also due to the thermal conductivity that drives the mass ablation of the shell material. The ablation process is characterized by the ablation velocity V_a, which is defined as the ratio of the mass ablation rate to the shell density, $V_a = \dot{m}/\rho_{sh}$. The larger the value of the ablation velocity, the larger the ablative stabilization.[3] Taking thermal smoothing and ablative stabilization into account, one can make a general statement that the higher the initial intensity of the drive laser pulse, the smaller the nonuniformities and the more stable the implosion. Indeed, the higher intensity tends to create the conduction zone in shorter time, reducing the laser imprint. In addition, the initial shock launched by the higher-intensity pulse is stronger, resulting in larger shock preheat. This re-duces the shell density, increasing the ablation velocity. Furthermore, a lower density leads to an increase in the shell thickness and a reduction in the perturbation feedthrough from the ablation front to the shell's rear surface (which becomes unstable during the deceleration phase of the implosion). There is a price to pay, however, for the greater stability. As the stronger shock propagates through the shell, it increases the shell entropy. A parameter (commonly used in the ICF community[1,2]) that characterizes the shell entropy during the implosion is the shell adiabat α. The adiabat is defined as the ratio of the shell pressure to the Fermi-degenerate pressure calculated at the shell density. Since the shell compressibility is reduced by an increase in the adiabat, the final compression ratio and the target neutron yield are also reduced. A common practice in designing direct-drive targets is to find the delicate balance between reduction in the target performance due to an increase in the adiabat and the increase in shell stability.

In optimizing the target design, one can take into consideration that the RT modes are surface modes peaked at the ablation surface of the shell. Therefore, to reduce the instability growth, it is sufficient to raise the adiabat only at the outer region of the shell, which ablates during the implosion. If the inner portion of the shell is kept on a lower adiabat, the shell and vapor compressibility will not be reduced during the final stage of implosion, and the neutron yields will be unaffected by this selective adiabat increase (adiabat shaping). New direct-drive designs proposed in the current work use adiabat shaping to improve the performance of the imploding shells. The idea of adiabat shaping using radiation preheat has already been implemented in an ignition target presented in Ref. 2. The designs described in this article use a different approach. The shell adiabat is shaped by launching a shock whose strength decreases as it propagates through the shell. This places an adiabat gradient directed toward the ablation front. Time variation in the shock strength is imposed by using an intensity picket in front of the main-drive pulse. The picket launches a strong shock that propagates through the shell. As the laser intensity drops at the end of the picket, the shocked material starts to expand and a rarefaction wave is launched toward

the shock. After the rarefaction and the shock coalesce, the shock strength decays, reducing the adiabat of the shock-compressed material.

The picket pulse shapes for the direct-drive (DD) ignition target designs were first proposed in Ref. 6. The main motivation for such pulses was to replace a continuous shell acceleration with an impulsive acceleration. The impulsive acceleration leads to a linear-in-time growth, replacing the exponential RT growth.

It would be premature, however, to make a conclusion about the shell stability based only on an analysis of the ablation velocity. A careful account of all additional sources of the perturbation growth prior to and during the shell acceleration is required. The analysis reported in this article reveals that introducing an adiabat gradient creates conditions for an additional instability. In the shaped-adiabat designs, the gradient in the entropy has the same sign as the effective acceleration, which excites the convective instability.[7] It is well known,[7] however, that the convective instability modes are internal modes (the eigenmode maximum is localized inside the shell), and the instability growth rates are lower than those of the classical RT instability. Although our analytical calculations and numerical simulations show that such an instability makes no significant contribution to the overall shell nonuniformity balance in the designs described here, care must be taken to control the seeding and the growth of the internal convective modes. In addition, the analysis reveals an "early time" RT growth (prior to the acceleration RT growth) at the ablator/main fuel interface during the transitional phase between the picket and the main drive pulse. Such a growth leads to a modification in the mode structure prior to the acceleration phase.

This article identifies the main advantages and possible disadvantages in using adiabat shaping in ICF target designs. The following sections (1) derive a time history of the material flow in a decaying shock configuration; (2) describe new DD designs for the OMEGA[8] and the National Ignition Facility's[9] laser systems and present the results of stability analysis of such designs; and (3) summarize the results of the experiments performed with the shaped-adiabat warm plastic targets.[10]

Propagation of a Decaying Shock

As described in the **Introduction**, new target designs are proposed using an intensity picket to shape the adiabat inside the shell. In this section we determine the adiabat profile by solving a simplified problem of shock propagation in the case of an impulsive applied pressure. We assume that a finite pressure p_p is applied during a time interval $0 < t < t_p$. At $t > t_p$ the applied pressure goes to zero. During the picket duration, a strong shock is launched into the shell. As the external pressure goes to zero, the shocked material starts to expand, launching a rarefaction wave in the direction of the initial shock. At $t = t_p + t_{rw}$ the rarefaction wave catches up with the shock, and the shock strength starts to decay. Therefore, by the time the shock breaks out at the rear surface, the adiabat at the shell's rear surface will be lower than the adiabat at the front surface. The problem of shock propagation in the case of the impulsive load has been considered previously,[11,12] and the solution was obtained using a self-similar analysis.[11] Such an analysis, however, is only valid asymptotically ($t \gg t_p$). Since there is a finite decrease in the entropy prior to the time when the solutions of Ref. 11 become valid, the self-similar treatment cannot predict the total entropy variation across the shell, so we must use a different approach to determine the adiabat profile.

Assuming that in the laboratory frame of reference the shock moves in the negative x direction with the velocity $U_s = \sqrt{(\gamma+1)p_s/(2\rho_0)}$, the hydrodynamic conservation equations can be combined to determine the time evolution of the pressure p_s at the shock front:

$$\frac{dp_s}{dt} = \frac{\gamma-1}{2\gamma-1}U_s(\partial_x p)_s, \qquad (1)$$

where γ is the ratio of specific heats and ρ_0 is the initial shell density. In writing Eq. (1) we used a strong-shock limit $p_s/p_0 \gg 1$, where p_0 is the initial shell pressure. Next, we must calculate the pressure gradient at the shock front. We accomplish this by considering a physically equivalent problem: instead of a decaying shock propagating through a uniform density (first problem), we consider a rarefaction wave propagating along the hydrodynamic profiles with finite density, pressure, and entropy gradients (second problem). These two problems will be equivalent if the hydrodynamic profiles of the second problem will satisfy the Hugoniot relations[7] at the shock position in the first problem. If the shock remains strong at all times, the compressed density right after the shock front remains constant, $\rho_s = (\gamma+1)/(\gamma-1)\rho_0$. Therefore, the Hugoniot relations must be satisfied in the second problem at the point where the local density is equal to ρ_s. To simplify the solution of the second problem near the shock front, we order $L_s^{-1} = \partial_x s/s \ll \gamma\partial_x \rho/\rho = \gamma L_\rho^{-1}$ (the large γ limit), where s is the shell entropy. This leads to an intro-

duction of the long-scale variables $T = t\delta$ and $X = x\delta$, where $\delta \sim L_\rho/(\gamma L_s) \ll 1$. Next, we expand the mass and momentum equations and all hydrodynamic functions in powers of δ and perform a multiscale analysis. Keeping only the zero-order terms in δ in the conservation equations yields the system $(v - \xi)\partial_\xi\rho + \rho\partial_\xi v = 0$, $(v - \xi)\partial_\xi v + c_s^2\partial_\xi\rho/\rho = 0$, where $\xi = x/(t - t_p)$ [the rarefaction wave is launched at $t = t_p$]. Solving the last system gives $(v - \xi)^2 = c_s^2$, where $c_s = \sqrt{\gamma p/\rho}$. For the rarefaction wave propagating in the negative x direction, we obtain $v = \xi + c_s$. Then, the pressure profile inside the rarefaction wave becomes

$$p = p_p\left(s_p/s\right)^{1/(\gamma-1)}\left[2c(X,T)/c_p(\gamma+1)\right.$$

$$\left. -(\gamma-1)/(\gamma+1)\xi/c_p\right]^{2\gamma/(\gamma-1)},$$

where $c_p = \sqrt{\gamma p_p/\rho_s}$, $s_p = p_p/\rho_s^\gamma$, and $c(X,T)$ is an undefined function of the long-scale variables. Taking the spatial derivative of pressure at the shock front, $\partial_x p \simeq \partial_\xi p/(t - t_p)$, yields

$$\partial_x \frac{p_s}{p_p} \simeq -\sqrt{\frac{p_s}{p_p}}\frac{2\gamma}{\gamma+1}\frac{1}{c_p(t - t_p)}. \qquad (2)$$

Observe that the gradient does not explicitly depend on the unknown function $c(X,T)$; this significantly simplifies the analysis. Substituting Eq. (2) back into Eq. (1) gives $dp_s/dt = -\beta p_s/(t - t_p)$ and $\beta = \sqrt{2\gamma(\gamma-1)/(2\gamma-1)}$, which leads to

$$\frac{p_s}{p_p} = \frac{\alpha_s}{\alpha_f} = \left(\frac{t - t_p}{t_{\rm rw}}\right)^{-\beta}, \qquad (3)$$

where $t_{\rm rw}$ is the rarefaction wave's propagation time from the outer surface of the foil to the shock front and α_f and α_s are the adiabat[1] at the front surface of the shell and shock front, respectively. It can be shown that the corrections to Eq. (3) due to the long-scale variations are small when $\gamma > 1.2$. Figure 93.14 compares Eq. (3) (dashed curve) with the results of numerical simulation (solid curve) using the one-dimensional Lagrangian code *LILAC*.[13] The figure shows evolution of the pressure at the shock front calculated for a 200-μm-thick DT foil driven by a 300-ps, 3.3×10^{14} W/cm^2 laser pulse ($t_p + t_{\rm rw}$

= 440 ps in this case). A good agreement between theoretical predictions and numerical results confirms the accuracy of Eq. (3). Figure 93.14 also plots the results obtained using the self-similar solution of Ref. 11 ($\beta = 0.78$) (dotted curve). Although the self-similar solution accurately predicts the shock pressure's decaying rate after $t = 1$ ns, the absolute value of the pressure (and the adiabat) is ~40% lower than the value obtained in the simulation.
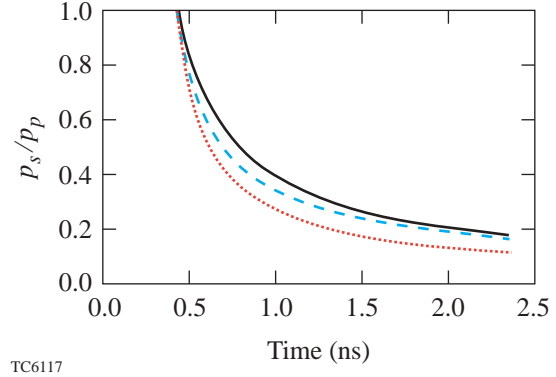

TC6117

Figure 93.14
Pressure at the shock front calculated using Eq. (3) (dashed curve), results of one-dimensional code *LILAC* (solid curve), and the self-similar solution of Ref. 11 (dotted curve). Calculations are performed for a 200-μm-thick DT foil driven by a 300-ps intensity picket.

Next, using Eq. (3) we calculate the entropy distribution inside the shell in terms of the mass coordinate. First, we introduce the mass m^* per unit area compressed by the shock during time interval $t = t_{\rm rw} + t_p$, $m^* = \rho_0 U_s^p(t_p + t_{\rm rw})$, where $U_s^p = \sqrt{(\gamma+1)p_p/(2\rho_0)}$. The rarefaction-wave propagation time $t_{\rm rw}$ can be related to the picket duration time t_p by equating the distance traveled by the shock (in the frame of reference of the compressed material) $d_s = (t_p + t_{\rm rw})U_{\rm sh}^p(\gamma-1)/(\gamma+1)$ to the distance traveled by the rarefaction wave $d_s = c_p t_{\rm rw}$. This gives $t_p/t_{\rm rw} = \sqrt{2\gamma/(\gamma-1)} - 1$. The fraction of mass dm overtaken by the shock during time dt is $dm = \rho_0 U_s dt$. This gives $dm/dt = (m^*/t_{\rm rw})\sqrt{\alpha_s/\alpha_f}/(1 + t_p/t_{\rm rw})$. With the help of Eq. (3), the solution of the last equation becomes

$$\alpha(m) = \alpha_f\left[\frac{2-\beta}{2}\sqrt{\frac{2\gamma}{\gamma-1}}\left(\frac{m}{m^*}-1\right)+1\right]^{-2\beta/(2-\beta)}. \qquad (4)$$

For a practical application, it is important to determine the duration t_p and the height p_p of the picket that gives the maximum adiabat ratio α/α_b at the beginning of the shell

acceleration (the onset of the RT-instability growth), where α_b = $\alpha(m_{sh})$ is the adiabat at the shell's rear surface and m_{sh} is the total shell mass. The target starts to accelerate soon after the shock breakout at the shell's rear surface. Therefore, to calculate the adiabat at the position of the ablation front at the beginning of the shell acceleration, we must calculate the fraction of the shell material ablated during the shock transit. For a constant applied pressure p_p, the shock transit time across the shell of thickness Δ_0 is $t_{shock} = \Delta_0 / \sqrt{(\gamma+1)p_p / (2\rho_0)}$. Then, using the scaling of the mass ablation rate

$$\dot{m}(g/cm^2/s) = 1.05 \times 10^6 I_{15}^{1/3}$$

and the ablation pressure[1] $p_p(Mbar) = 80.5 I_{15}^{2/3}$, we obtain the ablated DT mass during the shock propagation, $\Delta m = 0.2\, m_{sh}$. Here, I_{15} is the laser intensity in units of 10^{15} W/cm^2. Observe that since Δm does not depend on the applied pressure, we can use the derived ablated fraction also in the case of the picket pulse. Substituting $m = \Delta m$ into Eq. (4) we obtain the ablation-front adiabat α_{abl} at the beginning of shell acceleration:

$$\frac{\alpha_{abl}}{\alpha_b} = \left[\frac{(1-\beta/2)\sqrt{2\gamma/(\gamma-1)}(m_{sh}/m^* - 1) + 1}{(1-\beta/2)\sqrt{2\gamma/(\gamma-1)}(0.2 m_{sh}/m^* - 1) + 1} \right]^{2\beta/(2-\beta)} . (5)$$

Observe that α_{abl} is a monotonically growing function of m^*. Equation (4), however, is valid only for $m \geq m^*$, thus α_{abl} reaches the maximum value at $m^* = 0.2\, m_{sh}$,

$$\max(\alpha_{abl}) = \alpha_b \left[2(2-\beta)\sqrt{\frac{2\gamma}{\gamma-1}} + 1 \right]^{2\beta/(2-\beta)} = 6.3\, \alpha_b$$

for $\gamma = 5/3$. This shows that at the onset of the RT instability, the maximum ratio of the ablation front and rear-surface adiabat that can be achieved with a single picket pulse is 6. Taking into account that $V_a \sim \alpha^{3/5}$, this gives an increase in the ablation velocity by a factor of 3 at the beginning of the shell acceleration. The ablation velocity, however, decays in time since the ablation front moves into a region with a lower adiabat. Using

$$m^* = \rho_0 U_{sh}^p t_{rw} \sqrt{2\gamma/(\gamma-1)} = 0.2\, m_{sh} = 0.2\rho_0\Delta_0$$

leads to a relation between the applied impulsive pressure p_p, duration of the picket t_p, and the shell thickness Δ_0, $p_p t_p^2 \approx 9 \times 10^{-3} \rho_0 \Delta_0^2$. For DT shells, $\rho_0 = 0.25$ g/cm^3, and the picket pressure is $p_p = 6.3\, p_b$, where $p_b(Mbar) = 2.14\rho_s^{5/3}\alpha_b$ is the pressure at the shell's rear surface. Therefore, the optimum pulse duration becomes $t_p(ns) \sim 10^{-3} \Delta_0(\mu m)/\sqrt{\alpha_b}$. For a typical OMEGA cryo design $\Delta_0 \sim 80$ μm, and the optimum picket duration for $\alpha_b = 3$ is $t_p \approx 50$ ps. For the NIF DD designs with $\Delta_0 \approx 350$ μm, $t_p \approx 200$ ps. This estimate shows that the new target designs require short picket pulses to optimize the adiabat shape inside the shell. In the next section we study the effect of adiabat shaping on the perturbation growth in the OMEGA and NIF cryogenic target designs.

NIF and OMEGA Target Designs with Adiabat Shaping

Adiabat shaping is expected to reduce the growth rates of the RT-instability modes. The final mode amplitudes, however, depend not only on the growth rates but also on the initial seeds. Such seeds are determined by the surface roughness and the laser imprint amplified/reduced by the perturbation evolution during the early stage of the implosion when the first shock launched at the beginning of the laser pulse propagates through the shell. The perturbation amplification factor at the early stage depends on the details of a particular target design. In this section we study the effects of adiabat tailoring (in both the seeding and the RT-growth rates) in the cryogenic $\alpha = 3$ targets designed for the OMEGA and the NIF laser facilities. Here, α stands for the adiabat at the back of the shell. To avoid confusion, we refer to the OMEGA and NIF $\alpha = 3$ designs previously described in Ref. 14 as the standard designs. The designs presented in the current work will be referred to as picket designs. The standard designs have a very thin (1 μm for the OMEGA shells and 3 μm for the NIF shells) plastic overcoat required for DT-shell fabrication. These targets are driven by a laser pulse that consists of a constant-intensity foot ($I \sim 10^{13}$ W/cm^2) followed by the main drive pulse with $I_{max} \sim 10^{15}$ W/cm^2. The requirement for the very thin overcoat layers comes from the minimization of the early-stage perturbation growth factors. Such a growth is due to an impedance mismatch between plastic and DT ice that leads to an additional perturbation growth by a factor[15] $\sim e^{1.5\sqrt{kd_{CH}}}$, where k is the perturbation wave number and d_{CH} is the overcoat thickness. In the picket designs, such a requirement, as shown later, can be relaxed, and a thicker polymer overcoat is used to facilitate shell manufacturing and to increase the laser absorption. The overcoat thickness is determined by the requirement that the plastic layer be ablated by the beginning of the acceleration phase. This is done to take advantage of the higher ablation velocity of the lower-density DT ice. There is a negative side,

however, in an increased overcoat thickness: when the DT ice becomes the ablator, radiation from the plastic present in the hot corona streams through the ablator, preheating the main fuel. The picket designs, nevertheless, use thicker polymer layers (5 μm for OMEGA and 17 μm for the NIF) since our calculations show the beneficial overall effects of an increased overcoat thickness. The picket designs for OMEGA and the NIF are presented in Fig. 93.15. The laser pulse in both cases consists of a picket [we assume a Gaussian picket with FWHM (full width at half maximum) = t_p], an intensity rise, and the main-drive pulse with the maximum power P_{max}.

Shell thickness is determined by the implosion velocity and the laser energy. The minimum implosion velocity[1] required for ignition of large-aspect-ratio cryogenic targets is min (V_{imp}) ~ 3×10^7 cm/s. The implosion velocity in a robust ignition design must exceed this value in order to have excess kinetic energy at the time of ignition. Such a margin[14,16] helps to compensate for the effects of the shell nonuniformity. A larger value of the implosion velocity is also required to reduce the perturbation growth rates during the deceleration phase of implosion. As shown in Ref. 17, the ablation velocity during the deceleration phase is proportional to the hot-spot temperature to the power 5/2. The larger implosion velocity leads to a higher hot-spot temperature[16] (T_{hs} ~ V_{imp}) and larger ablative stabilization of the RT modes during the shell deceleration. Based on results of the stability analysis, we found that the implosion velocity for the direct-drive NIF targets should not be less than 4×10^7 cm/s. For the current design we choose

$V_{imp} = 4.3 \times 10^7$ cm/s. A given implosion velocity and the absorbed laser energy (which can be translated into the shell kinetic energy, taking into account the implosion efficiency of ~7%) uniquely determine the shell mass.

Shell radius is defined by minimizing the duration of the shell's coasting phase. Soon after the laser is turned off (end of the acceleration phase), the target starts to decompress: the front and rear surfaces expand with a local sound speed. The expansion of the back of the shell lasts until the main shock reflected from the shell center starts to interact with the incoming shell (beginning of the deceleration phase). Minimizing the time of the shell's free expansion (coasting phase) maximizes the final total ρR. This leads to a requirement on the shell radius: by the time the laser is turned off, the main shock must reach the shell center. If the shell radius is too small, on the other hand, the deceleration phase will begin while the laser is still on. The high pressure in the vapor will prevent, in this case, the shell from gaining the required implosion velocity; therefore, an effective transfer of the absorbed laser energy to the shell's kinetic energy will not be possible.

Laser pulse shape in the picket design is determined by several parameters: (1) rear-surface adiabat, which affects the target neutron yield and shell ρR (it also controls the stability during the deceleration phase), (2) the adiabat shape inside the shell, and (3) proper timing of all shocks and compression waves developed during the implosion. The first two parameters determine the picket peak intensity and picket duration
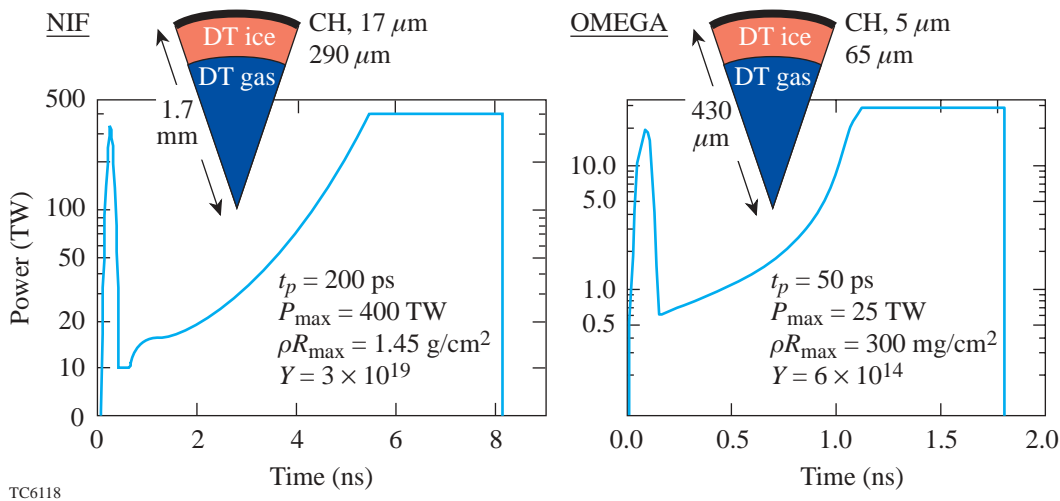

TC6118

Figure 93.15
Direct-drive, $\alpha = 3$ cryogenic target designs for the OMEGA and NIF laser systems.

(see the previous section). Meeting the third constraint on the pulse shaping requires accounting for all hydrodynamic waves that are launched during the implosion. Next, we summarize the main waves. First, a strong shock wave (SW_1) is launched by the picket at the beginning of the pulse. Then, as the intensity drops to a much lower level after $t = t_p$, a rarefaction wave (RW_p) starts to propagate through the shock-compressed material, and, as soon as the rarefaction catches the shock, the shock strength starts to decrease. The SW_1 sets up the shell adiabat for the entire acceleration phase (with a minor increase due to a radiation preheat and additional hydrodynamic waves). Later, the laser power ramps up to reach the maximum value P_{max}, and a compression wave or a weak shock is formed at the ablation front. To emphasize that such a wave should not turn into a strong shock (this limits the slopes of the intensity rise), we denote this wave as a compression wave (CW). As the SW_1 breaks out at the shell's rear surface, the surface starts to expand, launching a rarefaction wave (RW_b). While the RW_b travels from the rear surface toward the ablation front, it establishes some velocity, pressure, and density gradients. Each fluid element inside the RW_b is accelerated according to $dv/dt = -\partial_x p/\rho$, where p and ρ are the pressure and density of the fluid element. At the head of the rarefaction, ρ is equal to the shell density compressed by the SW_1 and CW. When RW_b reaches the ablation front, the density suddenly drops, creating a large acceleration gradient. This forms a local excess in the pressure that starts to propagate in the form of a compression wave along decreasing pressure and density profiles. A compression wave propagating along a decaying density turns into a shock (SW_2) inside the shell.[18] We want to stress here that SW_2 cannot be avoided. It will be created even for a constant-intensity pulse. The effect of SW_2 on the target performance, however, can be minimized by appropriately choosing the rise time of the laser pulse: the point where the laser reaches the maximum power must be between the SW_1 breakout at the rear surface and the RW_b breakout at the ablation front (in other words, the laser must reach the peak power while RW_b propagates through the shell). In addition, a proper timing of the pulse requires that, while traveling inside the shell, the SW_1 always be ahead of the CW. The time difference, however, between the breakout of the CW and SW_1 at the rear surface must not be larger than $\Delta t = c_s/(\Delta_0/16)$, where c_s is the average sound speed inside the shell compressed by the SW_1, and Δ_0 is the initial shell thickness.

Figure 93.15 shows the picket target designs, taking into account all the constraints on the shell size and pulse shape discussed above (for a better shell stability, the coasting phase

in the OMEGA design was extended). The OMEGA design reaches the implosion velocity $V_{imp} = 4.6 \times 10^7$ cm/s, peak of the total $\rho R_{max} = 300$ mg/cm^2, and it produces $Y = 6 \times 10^{14}$ neutrons. The NIF design has, correspondingly, $V_{imp} = 4.3 \times 10^7$ cm/s, $\rho R_{max} = 1.45$ g/cm^2, and $Y = 3 \times 10^{19}$ (gain = 55). Next, we study the stability of the designs presented in Fig. 93.15. We start by analyzing the perturbation growth rates.

1. Reduction in the Rayleigh–Taylor Growth Rates

The main motivation for the adiabat shaping is to increase the ablation velocity of the shell. Such an increase results in a reduction in the RT-growth rates. To separate the effect of the RT-growth-rate reduction from effects of the multiple material interfaces (which will be studied later), we consider a pure-DT shell (no polymer overcoat) driven by both a standard pulse and a picket pulse. The OMEGA all-DT target, equivalent to the design presented in Fig. 93.15, has an outer diameter of 430 μm and a shell thickness $\Delta_0 = 85$ μm. The pulse shape for the standard $\alpha = 3$ OMEGA design is taken from Ref. 14. Averaged over the time of shell acceleration, V_a increases from 4 μm/ns in the standard design to 6.5 μm/ns in the picket design. The RT-growth rates are estimated by substituting the ablation-front trajectories R_a obtained from the 1-D simulation into the fitting growth-rate formula,[20] $\Gamma_{RT} = 0.94\sqrt{kg} - 2.6\,kV_a$. Since the fitting formula uses time-independent planar geometry variables, g, $k = \ell/R_a$, and V_a are averaged over the duration of the acceleration phase. Figure 93.16 shows the results of the fitting formula applied to the two designs. Next, a series of two-dimensional simulations using the Lagrangian code *ORCHID*[21] was performed to calculate the growth rates of the RT modes. The instability was seeded by applying a 1% laser-intensity modulation.
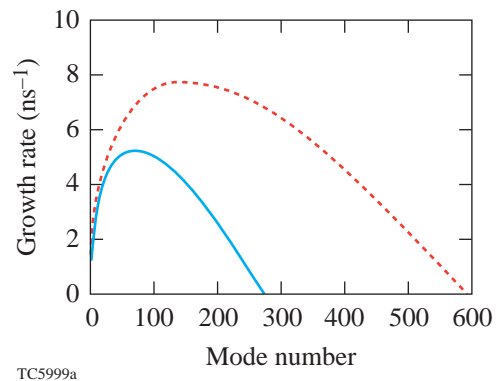
TC5999a

Figure 93.16

Rayleigh–Taylor growth rates for the standard (dashed curve) and the picket (solid curve) OMEGA designs.

Figures 93.17(a) and 93.17(b) compare the results of simulations (solid and dotted lines) with theoretical prediction (dashed straight lines) for mode numbers $\ell = 60$ and $\ell = 100$. Simulations exhibit lower growth rates at the beginning of the acceleration phase and higher growth rates at the end of acceleration. This is mainly due to a wave number variation during shell compression and, in the case of the picket design, lower ablation velocity at the end of the laser pulse. Averaged over the duration of the acceleration phase, however, simulations agree reasonably well with the result of the fitting formula. According to Fig. 93.16, the cutoff mode number is expected to be reduced from $\ell_{cut} \approx 600$ for the standard pulse to $\ell_{cut} \approx 280$ for the picket design. In Fig. 93.17(c) we plot the temporal evolution of the mode $\ell = 300$, which is predicted to be stable for the picket case. Indeed, the simulations clearly show the mode growth in the standard design and the mode stabilization in the picket design. Based on the results of 2-D simulations we conclude that the reductions in the growth rates due to adiabat shaping are in good agreement with the analytical predictions. Next, we turn our attention to the seeding of the RT modes in the picket design with multiple layers.

2. Seeding of the Rayleigh–Taylor Modes in Multilayer Targets

To calculate the nonuniformity evolution throughout the implosion, it is essential to accurately predict the initial conditions for the RT-instability growth. Such initial conditions, in turn, depend on how the laser imprint and surface roughness evolve prior to the onset of the RT instability (prior to the RW_b breakout at the ablation front). In this subsection we estimate the growth factor of the initial perturbation seeds during the early stage of implosion.

The RW_p (see p. 23) launched into the compressed material establishes a pressure profile decaying toward the ablation front. This creates pressure and density gradients of opposite directions at the CH/DT interface. Thus, a short period of the classical RT growth ("early time" RT growth) occurs at the interface. Such a period lasts until the CW reaches the interface and changes the sign of the pressure gradient. The amplification of the interface perturbations (seeded by the distorted SW_1) can be estimated from the following considerations: The interface between the heavier CH and lighter DT is a Lagrangian point moving with a local fluid velocity. Since the pressure profile across the interface is established by the rarefaction wave RW_p, the interface acceleration is an acceleration of a Lagrangian point inside the rarefaction wave. Next, we consider a rarefaction wave traveling along a stationary uniform density $\bar{\rho}$ and pressure $\bar{p}$. The solution of the hydrodynamic equations in this case written in the Lagrangian coordinates has the form[18] ($\gamma = 5/3$):

$$\rho = \bar{\rho}\left(\frac{x_0}{\bar{c}t}\right)^{3/4}, \quad p = \bar{p}\left(\frac{x_0}{\bar{c}t}\right)^{5/4}, \quad (6)$$

where $\bar{c} = \sqrt{\gamma\bar{p}/\bar{\rho}}$. The time coordinate in the last equation is shifted to the beginning of the rarefaction wave propagation. The acceleration of a Lagrangian point is calculated by taking the derivative of the pressure with respect to the Lagrangian
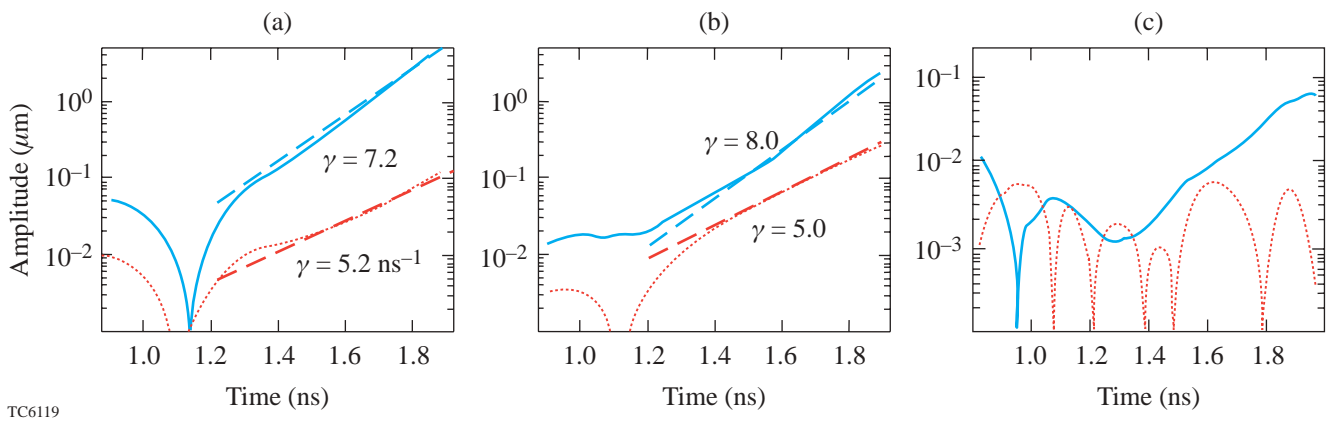

(a)   (b)   (c)

TC6119

Figure 93.17
Mode evolution for (a) $\ell = 60$, (b) $\ell = 100$, and (c) $\ell = 300$. Numerical results are shown with the solid (standard design) and dotted (picket design) lines; the predictions of the fitting formula[20] are indicated by the dashed straight lines. Calculations are performed for the OMEGA $\alpha = 3$ design.

variable x_0 (at time $t = 0$, the rarefaction wave is at $x_0 = 0$):

$$g = -\frac{1}{\bar{\rho}}\frac{\partial p}{\partial x_0} = -\frac{3}{4}\frac{\bar{c}^2 x_0^{1/4}}{(\bar{c}t)^{5/4}}. \tag{7}$$

Next, we take x_0 to be the polymer thickness (Lagrangian position of the CH/DT interface) at the beginning of the RW_p propagation, $x_0 = \Delta_{CH} = c_{CH} t_r$, where t_r is the RW_p breakout time at the CH/DT interface, and c_{CH} is the sound speed of the shock-compressed CH. Simulations show that $\Delta_{CH} \simeq d_{CH}/6$, where d_{CH} is the initial overcoat thickness (the SW_1 compresses the plastic layer by a factor of 4; additional reductions in thickness are due to the mass ablation and adiabatic compression of the CH layer during the picket rise). The parameter $\bar{c}$ in this case is $\bar{c} = c_{CH} = \sqrt{\gamma p_{CH}/\rho_{CH}}$, where p_{CH} is the pressure at the shock front in CH and $\rho_{CH} = (\gamma+1)/(\gamma-1)\rho_{CH}^0$ is the shock-compressed CH density. Next, to find the perturbation growth fac-tor at the interface, we must solve the RT evolution equation (including decompression effects):

$$\frac{d}{dt}\left[\frac{d_t(\rho\eta)}{\rho}\right] - A_T k g\eta = 0, \tag{8}$$

where η is the CH/DT interface modulation amplitude, k is the wave number, and, according to the *LILAC* simulations, $A_T \simeq 1/3$. The Wentzel–Kramers–Brillouin (WKB) solution[22] of Eq. (8) has the form

$$\eta = \tau^{11/16}\left(Ae^\zeta + Be^{-\zeta}\right),$$

where $\zeta = 4/3\sqrt{k\Delta_{CH}}\,\tau^{3/8}$ and $\tau = c_{CH}t/\Delta_{CH}$. Equation (8) is subject to the initial conditions at the onset of the perturbation growth: $\eta(t = t_r) = \eta_0$ and $\dot{\eta}(t_r) = \dot{\eta}_0$. These conditions can be defined from the following considerations: If the interface perturbation is seeded by a nonuniform shock with a modulation amplitude η_s, then η_0 and η_s are related as $\eta_0 = \eta_s U_{ps}^{DT}/U_s^{CH}$, where

$$U_{ps}^{DT} = \sqrt{2/(\gamma+1)\,p^{DT}/\rho_{DT}^0}$$

is the post-shock fluid velocity in DT and

$$U_s^{CH} = \sqrt{p_p(\gamma+1)/2/\rho_{CH}^0}$$

is the shock velocity in CH. Because of the density jump across the CH/DT interface, the pressure behind the SW_1 drops as the shock crosses the interface. The transmitted pressure p_{DT} must satisfy the following equation derived from the matching conditions across the interface:

$$\sqrt{\Sigma} - \sqrt{\frac{\rho_{DT}^0}{\rho_{CH}^0}} = \sqrt{\frac{2\gamma}{\gamma-1}\frac{\rho_{DT}^0}{\rho_{CH}^0}}\left(1 - \Sigma^{\frac{\gamma-1}{2\gamma}}\right),$$

where $\Sigma = p_{DT}/p_p$. Substituting $\rho_{DT}^0 \simeq \rho_{CH}^0/4$, the last equation yields $p_{DT} \simeq 0.45\,p_p$; thus the transmitted pressure is one-half of the initial drive pressure. Thus, the initial interface amplitude becomes $\eta_0 \simeq \eta_s$. It is interesting to observe that the initial interface perturbation is approximately equal to the shock modulation amplitude. To calculate the initial velocity perturbation $\dot{\eta}_0$ we must take into account that the RW_p in the designs presented in Fig. 93.15 catches with the SW_1 inside the plastic, very close to the CH/DT interface. Thus, we can approximate that the interface starts to accelerate with g, defined by Eq. (7), right after the SW_1 crosses the interface. The velocity perturbation gained by the interface during time interval Δt is $\dot{\eta}_0 = g\Delta t$, where $\Delta t = \eta_s/U_s^{CH}$ is the time of the shock propagation across the amplitude η_s; then, $\dot{\eta}_0 \simeq 0.42\,\eta_s c_{CH}/\Delta_{CH}$. If the perturbations are seeded by the outer-surface roughness and the initial amplitude of the front ripple is a_0, then the shock amplitude[23] evolves according to

$$\eta_s(t) = a_0\left[J_0\left(kc_{CH}t/\mu\right) + 2/3\,J_2\left(kc_{CH}t/\mu\right)\right],$$

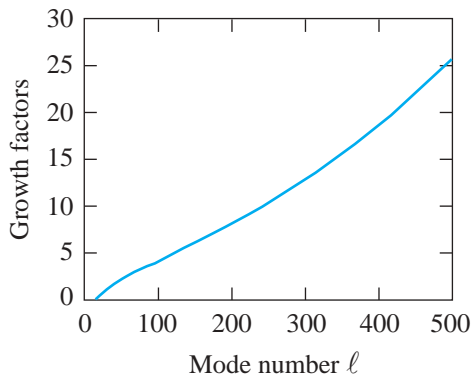where $J_0(x)$ and $J_2(x)$ are Bessel functions of zero and second orders, respectively, and

$$\mu = 1\bigg/\sqrt{1 - \left(U_s^{CH}/4c_{CH}\right)^2} \simeq 1$$

in the strong shock limit. Approximating the Bessel functions with their envelopes gives $J_0(z) + 2/3 J_2(z) \simeq \sqrt{2/(9\pi z)}$, where z calculated at the SW_1 breakout time at the interface is $z \simeq kd_{CH}/2$. Collecting all the terms together, the perturbation growth factor $GF = \eta(t)/a_0$ becomes
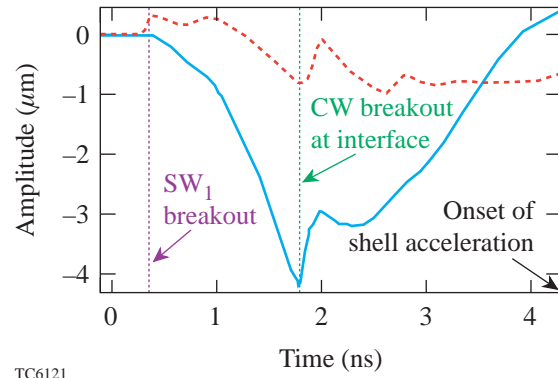
$$GF = \frac{0.38}{\sqrt{kd_{CH}}}\left(\frac{t}{t_r}\right)^{11/16}$$

$$\times\left(\cosh\sigma - \frac{0.8}{\sqrt{kd_{CH}}}\sinh\sigma\right), \qquad (9)$$

where $\sigma = 0.54\sqrt{kd_{CH}}\left[(t/t_r)^{3/8}-1\right]$. The perturbations imposed at the CH/DT interface by the perturbed SW_1 grow until the CW reaches the interface and changes the sign of the pressure gradient. Figure 93.18 plots the GF calculated for the NIF design presented in Fig. 93.15 ($t/t_r \sim 40$). The mode number ℓ is defined as $k = \ell/R_0$, where $R_0 = 1700\ \mu$m is the initial outer shell radius. The amplification in the mode amplitude, for the mode numbers of interest to ICF, varies from 1 to 30, but only a fraction of this amplitude seeds the RT mode at the onset of the target acceleration. This is partially due to the interface amplitude compression by the CW. An additional reduction comes from the coupling of the interface ripple to the ablation front, which is stabilized by the dynamic overpressure effect.[24] Figure 93.19 illustrates the reduction in the interface amplitude prior to the target acceleration. The interface modulation evolution is calculated using 2-D *ORCHID* simulations with an imposed initial outer-surface perturbation. The dashed line represents the behavior of mode $\ell = 100$ with $a_0 = 0.5\ \mu$m, and the solid line corresponds to $\ell = 300$ with $a_0 = 0.2\ \mu$m. The SW_1 breaks out at the CH/DT interface at 0.4 ns. At this time the interface modulation jumps to the value of the shock ripple amplitude (the shock modulation for $\ell = 300$

Figure 93.19
Evolution of the CH/DT interface modulation for $\ell = 100$ (dashed line) and $\ell = 300$ (solid line) prior to shell acceleration.

changes sign at $t = 0.4$ ns; therefore the plot shows the growth of this starting from zero amplitude). Although the short wavelengths experience a larger growth due to the early RT instability, their amplitudes are substantially reduced by the time of shell acceleration. The conclusion one can draw from this analysis is that the early RT growth of the CH/DT interface perturbations does not amplify significantly the seeds for the acceleration RT instability. Even if such amplification by a factor of several will occur, the perturbations will be substantially reduced by high ablation velocity (the adiabat has the largest value at the interface) when the ablation front crosses the CH/DT interface.

3. Convective Instability

It is well known that in the presence of the entropy gradient inside the shell, a convective instability develops if the effective acceleration and the entropy gradient are in the same direction.[7] Such an instability has been studied by several researchers in the past.[7,25] The following are important results of these studies: (1) In the classical RT case (no ablation) with negligibly small light-fluid density ($A_T \sim 1$), the convective mode is totally decoupled from the RT mode, and the RT-growth rate is $\gamma = \sqrt{kg}$, regardless of the adiabat shape (assuming a sharp interface between lighter and heavier fluids). (2) The growth rate of the convective modes is always smaller than the growth of the RT modes. The growth rates of the modes excited in the shell can be derived by combining the conservation equations into a single differential equation for the x component of the fluid velocity v (x coordinate is chosen in the direction of the acceleration g):

Figure 93.18
Growth factors of the "early time" RT instability in the NIF picket design.

$$\left(\Gamma^2 v - g\frac{dv}{dx}\right) = \left[c_s^2 \frac{d}{dx} + (\gamma - 1)g\right]$$

$$\times \left(\Gamma^2 + k^2 c_s^2\right)^{-1} \left(\Gamma^2 \frac{dv}{dx} - k^2 g v\right), \quad (10)$$

where k is the wave number, Γ is the perturbation growth rate, and $c_s = \sqrt{\gamma p/\rho}$ is the sound speed. In writing Eq. (10) the ablation effects were neglected. If $x = 0$ at the fluid interface and x is negative inside the shell, the pressure continuity condition at the interface reads as

$$p(\eta) = p_0(0) + \tilde{p}(0) + (dp/dx)\eta = p_0(0),$$

where $\tilde{p}$ is the pressure perturbation, p_0 is the equilibrium pressure, and η is the interface modulation amplitude. The velocity at the interface is related to the distortion amplitude as $v(0) = \Gamma\eta$; in addition, we write $dv/dx|_{x=0} = \mu k v(0)$, where μ is an undetermined constant. The pressure continuity in this case reduces to the simple relation

$$\Gamma = \sqrt{\frac{kg}{\mu}}. \quad (11)$$

It is easy to show that the solution $v \sim e^{kx}$ and $\Gamma = \sqrt{kg}\,(\mu = 1)$ satisfies Eq. (10); thus, the classical RT mode grows with $\Gamma = \sqrt{kg}$, regardless of the entropy profile inside the shell. As shown in Ref. 7, however, for all other modes that can be excited in the shell (the internal convective modes), $\mu > 1$ and the growth rates are smaller than $\sqrt{kg}$. In the ablative case, the growth rates of the RT instability are significantly reduced by the ablation. For the DT ablator, the fitting formula that reproduces the results of the self-consistent theory has the form[20] $\Gamma_{RT} = 0.94\sqrt{kg} - 2.6\,kV_a$. Near the cutoff wave number, where Γ_{RT} vanishes, the growth of the convective modes could exceed the RT growth. It is important, therefore, to study the internal mode growth in such a regime.

We begin the analysis by determining the spatial dependence of the adiabat for the picket designs shown in Fig. 93.15. The shell entropy $s(x)$ calculated using the 1-D simulations can be fitted with a power law $s(x) = s_0\left[1 - x/(\beta_s L_{sm})\right]^{-\beta_s}$, where L_{sm} (the minimum entropy gradient scale length) and the power index β_s are determined from the fitting procedure. The x coordinate is negative inside the shell, so $s(x)$ decreases

from the interface toward the back of the shell. Next, we solve Eq. (10) to find the eigenvalue μ, imposing the condition of finite v at the back of the shell. Near the RT cutoff, the condition $kL_{sm} \gg 1$ is satisfied, and Eq. (10) can be greatly simplified:

$$v'' - k^2 Q(x)v = 0, \quad Q(x) = 1 - \frac{\mu}{\gamma k L_s}, \quad L_s = L_{sm} - \frac{x}{\beta_s}. \quad (12)$$

Here, prime denotes the spatial derivative. In solving Eq. (12) we assume $\mu \gg 1$. This assumption will be verified later. Observe that Q is a decaying function of x; therefore the solution of Eq. (12) depends on the sign of Q inside the shell. It is easy to show that Q cannot be positive everywhere in the shell. Indeed, to satisfy the boundary condition at the shell's back, we must keep only the exponentially decaying solution

$$v_{WKB} \sim Q^{-1/4} \exp\left[k\int^x \sqrt{Q(y')}\,dy'\right],$$

where v_{WKB} is obtained using the WKB approximation. But such a solution does not satisfy the boundary condition at $x = 0$, $v'/v = k\mu$. Thus, Q must be negative somewhere in the shell. Next, we distinguish the following two cases: (1) Q changes sign at point $x = \bar{x}$, (2) Q is negative everywhere. In case (1), solution of Eq. (12) in the region where $Q > 0$ is $v = v_{WKB}$. In the vicinity of $x = \bar{x}$, the WKB approximation breaks down and Eq. (12) must be solved by expanding Q in the Taylor series,

$$Q = Q_0 - Q_1 k(x - \bar{x}),$$

where $Q_0 = 1 - \mu/\left[\gamma\left(kL_{sm} - k\bar{x}/\beta_s\right)\right] = 0$, and $Q_1 = \gamma/(\mu\beta_s)$. Then, the solution of Eq. (12) that matches v_{WKB} at $\tau \to \infty$ becomes $v_{in} \sim Ai(\tau)$, where $Ai(\tau)$ is the Airy function and $\tau = kQ_1^{1/3}(\bar{x} - x)$. We will show later that $|Q_1 k\bar{x}| \ll 1$ and the Taylor expansion of Q is still valid near $x = 0$. The boundary condition $v'/v = \mu k$ can be applied in this case to v_{in}. Using the expansion of the Airy function for the large negative arguments, the boundary condition reads as

$$\frac{1}{4\tau_0} + \sqrt{\tau_0}\,\tan\left(\frac{2}{3}\tau_0^{3/2} - \frac{\pi}{4}\right) + \mu^{4/3}\left(\beta_s/\gamma\right)^{1/3} = 0, \quad (13)$$

where $\tau_0 = \beta_s^{2/3}\left(\mu/\gamma - kL_{sm}\right)\left(\gamma/\mu\right)^{1/3}$ is the value of $-\tau$ at the density jump ($x = 0$). Since $\mu \gg 1$ (by assumption), the

right-hand side of Eq. (13) is large, and the equation can be satisfied only if the argument of the tangent is close to $\pi/2$. This defines τ_0, $(2/3)\tau_0^{3/2} \simeq 3\pi/4 + \pi n$, $n = 0, 1, 2$. Substituting the definition of τ_0 into the last equation leads to $\beta_s^2 \gamma(\mu/\gamma - kL_{sm})^3 = 9\pi^2(3/4 + n)^2 \mu/4$, which has the following solution:

$$\mu = \gamma kL_{sm} + \frac{\gamma}{4\beta_s}\left[9\pi^2(3 + 4n)^2 \beta_s kL_{sm}\right]^{1/3}, \ n = 0, 1, 2. \quad (14)$$

Observe that $\mu \gg 1$ for the short-wavelength modes considered here, in agreement with the initial assumption. Also, $|kQ_1\bar{x}| \sim (kL_{sm})^{-2/3} \ll 1$, which validates the Taylor expansion of Q near $x = 0$. Using Eq. (14), the growth rate $\Gamma = \sqrt{kg/\mu}$ takes the form

$$\Gamma = \sqrt{\frac{g}{\gamma L_{sm}\left\{1 + \left[\frac{9\pi(1 + 4n/3)}{8\beta_s kL_{sm}}\right]^{2/3}\right\}}}. \quad (15)$$

Next, we recall that Eq. (15) is valid only if Q changes sign inside the shell, i.e., $-d < \bar{x} < 0$, where d is the shell thickness. Such a requirement puts an upper limit on values of μ: $\mu < \gamma k(L_{sm} + d/\beta_s)$; using Eq. (14), the last condition reads as $n < (2\beta_s kL_{sm}/3\pi)(d/\beta_s L_{sm})^{3/2}$. The number n has a simple meaning: n indicates how many times the eigenmode changes sign inside the shell. To calculate the number n for the ICF target, we must recall that the internal modes are seeded only by the vorticity inside the shell.[7] In the ICF experiments the vorticity is induced either by the rippled shock propagating from the ablation front or by the rippled rarefaction wave in the case of the initial inner-surface roughness (feedout). In both cases the imposed vorticity oscillates inside the shell, and the characteristic spatial frequency of such oscillations is of the order of the perturbation wavelength. As an example, let us consider the case of the rippled shock. If a_0 is the initial outer-surface amplitude of the mode with the wave number k, the shock creates the shell vorticity[23,24] Ω_0 according to

$$\Omega_0 = i(\nabla \times \mathbf{v})_z = -kv_x - i\partial_x v_y$$

$$\approx \frac{3}{2}k^2 a_0 c_s\left[J_1(\zeta) + \frac{1}{2}J_3(\zeta)\right], \quad (16)$$

where $\zeta = k\Delta_0/2(m/m_{sh})$, $J_1(\zeta)$ and $J_3(\zeta)$ are the Bessel functions, m is the mass coordinate inside the shell, m_{sh} is the total shell mass, and Δ_0 is the initial shell thickness. Taking into account that 1/5 of the initial shell material is ablated by the time the shell accelerates (see the **Propagation of a Decaying Shock** section), $\zeta_{max} = 2k\Delta_0/5$. Using Eq. (16) and approximating $J_m(\zeta) \sim \sin(\zeta - m\pi/2 - \pi/4)$, it is easy to calculate the number of zeros in Ω_0: $N_0 \sim 2k\Delta_0/(5\pi)$. Taking $n = N_0$, the validity condition of Eq. (15) becomes

$$\frac{\Delta_0}{d} < \frac{5}{3}\sqrt{\frac{d}{\beta_s L_{sm}}}. \quad (17)$$

This condition is not satisfied for the target designs presented in Fig. 93.15 [$\Delta_0/d \sim 10$ (shell is compressed by the shock SW_1 and the compression wave CW), $d \simeq 8 \ \mu m$, $L_{sm} \simeq 5.4 \ \mu m$, and $\beta_s = 0.5$ for the OMEGA picket design]. Thus, to calculate the convective instability growth rate we must consider the second case when Q is always negative inside the shell.

If $Q < 0$, the WKB solution of Eq. (12) takes the form

$$v = \frac{A}{Q_-^{1/4}}\cos\left(k\int_0^x \sqrt{Q_-(y')}dy'\right)$$

$$+ \frac{B}{Q_-^{1/4}}\sin\left(k\int_0^x \sqrt{Q_-(y')}dy'\right), \quad (18)$$

where $Q_- = -Q > 0$ and A and B are constants of integration. The boundary condition at $x = 0$ relates $B \approx A\mu/\sqrt{Q_-(0)}$. To define the boundary condition at $x = -d$, we must keep in mind that both ρ and c_s vanish at the rear surface. Then, the solution that does not blow up at $x = -d$ must satisfy $v'(-d)/v(-d) = \mu k(\gamma - 1)/\gamma$ [this condition can be easily derived directly from Eq. (10)]. Applying the latter condition to solution (18) gives, in the limit of large μ,
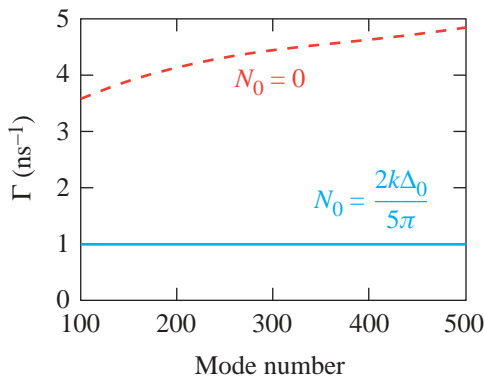
$$k\int_{-d}^0 \sqrt{\frac{\mu}{\gamma kL_s(x)} - 1} \ dx = n\pi, \ n = 1, 2... \quad (19)$$

Performing integration in the last equation and substituting $n = N_0$, we determine μ. Then, the growth rate $\Gamma = \sqrt{kg/\mu}$ becomes

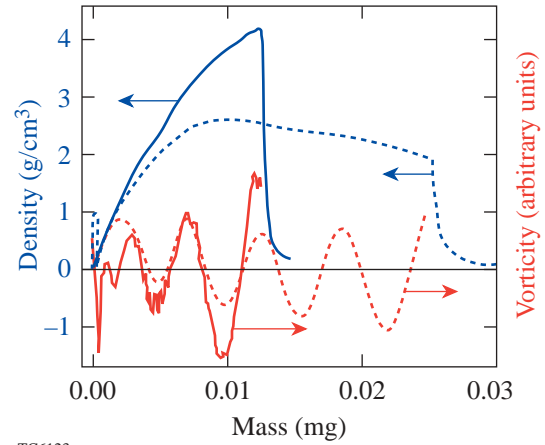$$\Gamma \simeq \sqrt{\frac{g}{\gamma L_{sm} \Sigma}},$$

$$(20)$$

$$\Sigma = \frac{\left(d/\sqrt{2}\beta L_{sm}\right)^2 + \left(\Delta_0/5\beta L_{sm}\right)^2}{\left(\sqrt{1 + d/\beta L_{sm}} - 1\right)^2} - \frac{1}{2}\sqrt{1 + \frac{d}{\beta L_{sm}}}.$$

Figure 93.20 plots the growth rates calculated for the OMEGA picket design using Eqs. (15) ($n = 0$, dashed line) and (20) (solid line). Observe a strong reduction in the growth rate due to the vorticity oscillations. We want to emphasize here that Eq. (20) is valid only if condition (17) is not satisfied. It is possible, however, to steepen the adiabat profile (by introducing a second picket in the laser pulse, for example), reducing the minimum scale length L_{sm} and increasing the compressed shell thickness d (the larger adiabat at the ablation front will lead to a decrease in the shell density). Equation (17) will be satisfied in this case, and Eq. (15) with $n = N_0$ must be used to calculate the growth rate. To validate the result of the performed analysis of the convective mode evolution, we carried out a series of single-mode 2-D *ORCHID* simulations imposing modulation on the outer surface of the shell. Figure 93.21 shows a plot of the density and vorticity as functions of the mass for $\ell = 300$ in the OMEGA picket design (Fig. 93.15). The dashed line represents the beginning of acceleration phase, and the solid line corresponds to the end of the acceleration phase (the mass is reduced because of the ablation). The vorticity amplitude has grown by a factor of 2 during the shell acceleration, which is in agreement with Eq. (20) (the acceleration phase in the OMEGA design lasts for 0.8 ns).

TC6122

Figure 93.20
Growth rate of the internal convective mode with (solid line) and without (dashed line) vorticity oscillation inside the shell.

TC6123

Figure 93.21
Mass density and vorticity calculated at the beginning (dashed line) and the end (solid line) of the acceleration phase.

In conclusion, Fig. 93.20 suggests that there is no significant amplification of the outer-surface distortions due to the convective instability (the growth factor is less than 3 for the entire mode spectrum). One needs to take the results of the present analysis with great caution. We did not address the question of how the internal mode can affect the growth of the RT modes. This issue will be studied in future work. Our simulations, however, indicate that even if such coupling exists, it does not significantly modify the RT growth for the designs described in Fig. 93.15. The conclusions could be different for other shaped-adiabat designs.

4. Multimode Results

The analysis performed in Subsections 1–3 gives an estimate for only the single-mode growth factors experienced by the perturbations during the implosion. To make a conclusion about the shell integrity for a particular target design, one must carry out multimode calculations, taking into account the realistic spectra of the surface roughness and the laser-intensity nonuniformity. Stability analyses of the direct-drive cryogenic targets reported in the past[14,19] reveal that the laser imprint is the dominant source for a potential shell breakup during the acceleration phase. To study the effect of the adiabat shaping on the shell integrity, we performed a set of multimode *ORCHID* simulations. First, we discuss the simulation results for the OMEGA cryogenic targets (dimensions are shown in Fig. 93.15) driven by the standard and picket pulses. A single-beam laser nonuniformity spectrum is evaluated for a static DPP (distributed phase plate) speckle. Then, an overlap of 12 OMEGA beams and two polarizations at any spot on the capsule are assumed. The effect of the two-dimensional SSD

(smoothing by spectral dispersion) beam-smoothing technique[26] is modeled by employing a "flipping" approximation: the sign of the laser perturbation is randomly chosen every correlation time t_c, where $t_c = \left[\Delta v \sin(k\delta/2)\right]^{-1}$, δ is the speckle size ($\delta = 2.35$ μm for the OMEGA), $\Delta v = 1$ THz is the laser bandwidth, and k is the perturbation wave number. Averaged over time T, the single-beam rms nonuniformity σ for a constant-intensity laser pulse decays in time as $\sigma \sim \sigma_0 \sqrt{t_c/T}$. Because of a finite maximum angular spread $\Delta\theta$ of the light propagating through the laser, the averaged mode amplitude cannot be reduced to the levels below the asymptotic limit. This limit is inversely proportional to the square root of the number of statistically independent speckle patterns

$$N_{stat}(\lambda) = \left(4S_{max}^x/\lambda\right)\left(4S_{max}^y/\lambda\right),$$

where λ is the nonuniformity wavelength, $S_{max}^{x(y)} = F\Delta\theta^{x(y)}$ is the maximum spatial shift in the $x(y)$ direction, $F = 180$ cm is the focal length, and $\Delta\theta^x = 50$ μrad and $\Delta\theta^y = 100$ μrad for the OMEGA laser system. The asymptotic limits are modeled in the flipping approximation by selecting only N_{stat} independent choices for the sign of the nonuniformity amplitude. Snapshots of the shell isodensity contours for the standard and the picket designs are shown in Figs. 93.22(a) and 93.22(b), respectively. The shell has moved the same distance (~100 μm) in both designs. The plots reveal a dramatic reduction in shell
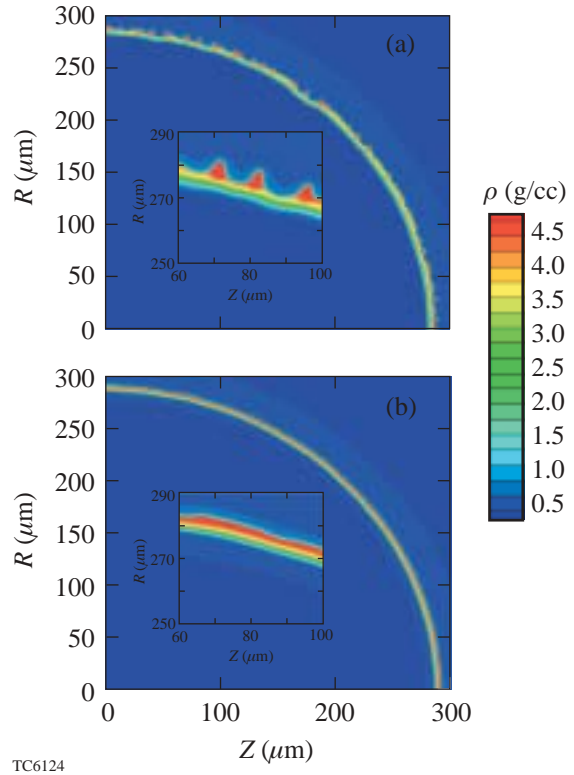
Figure 93.22
Isodensity contours of the (a) standard and (b) picket OMEGA $\alpha = 3$ designs. At the time shown on the plots, the shell has moved 100 μm in both designs.
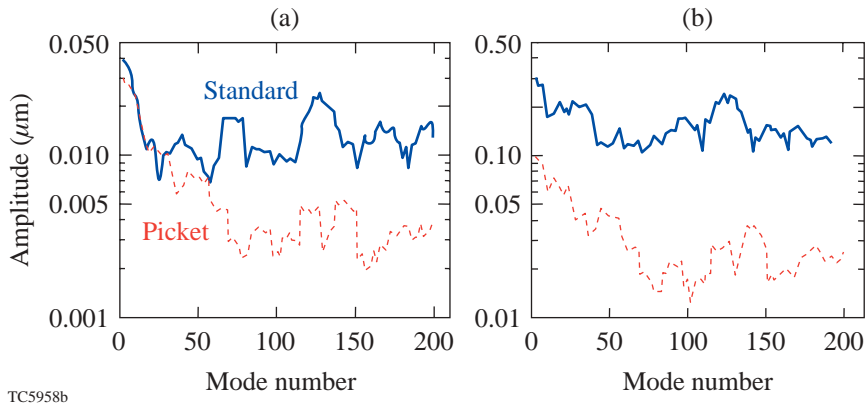
TC6124

Figure 93.23
Mode spectra for the standard (solid line) and picket (dashed line) OMEGA $\alpha = 3$ designs (a) at the beginning of acceleration phase and (b) at the time shown on Fig. 93.22(b).

TC5958b

nonuniformity in the picket design. We also emphasize that the picket reduces not only the perturbation growth rates but also the laser imprint.[27] Figure 93.23(a) plots the mode spectrum at the beginning of the acceleration phase for both designs. As shown in the plot, the picket reduces the initial amplitudes by a factor of 2.5 to 3 for the modes with $\ell > 50$. Comparing the mode amplitudes for the picket and standard designs at the time shown in Fig. 93.22 [see Fig. 93.23(b)], we observe that the separation between the two spectral lines is clearly increased (amplitudes in the picket designs are smaller by a factor of 10 for $\ell > 50$), indicating a slower RT growth in the picket design. A reduction in the growth of the low-ℓ modes is also noticeable. This is due to the ablation effects in a finite-thickness shell (for details see Ref. 28). The numerical simulations of the NIF cryogenic target design show a similar trend: shell nonuniformities are highly reduced in the picket design compared to the standard design. Although detailed multimode simulations including all the nonuniformity sources (surface roughness, laser imprint, and power imbalance) are still in progress, a preliminary analysis reported in this article indicates a substantial improvement in the shell uniformity by using laser-induced adiabat shaping.

Picket Pulse Experiments

To test the effect of the adiabat shaping on the performance of the imploding shells, a series of experiments[10] were carried out on the OMEGA laser system. The experiments were performed on 33-μm thick, 905-μm-diam, D_2-filled polysty-rene shells, filled to a pressure of 3 and 15 atm. Two pulse shapes [Fig. 93.24(a)] were used to compress the shells with a low adiabat ($\alpha = 2$) at the fuel/pusher interface. The standard pulse has a 1-TW, 700-ps-long foot followed by the main pulse with a peak power of 20 TW. The picket design has a narrow, 100-ps-FWHM (full width at half maximum) Gaussian picket combined with the main drive pulse described above. The adiabat in the standard pulse varies from 2 to 2.5; the adiabat at the ablation front in the picket design was raised to 4. There was also an increase in the adiabat at the rear surface in the picket design. Analysis performed using the stability post-processor[28] indicated that the shell in the standard design was broken due to the perturbation growth, while the shell in the picket design remained intact during the shell implosion. The experimental results are summarized in Fig. 93.24(b). The plot compares the experimental yield against the 1-D *LILAC* prediction. Observe that the predicted yields for the picket design were slightly reduced for both fill pressures, while the experimental yields grew by a factor of 2.5 for the 15-atm fill and by a factor of 2 for the 3-atm fill. The ratio of the experimental yield to the predicted 1-D yield grew from 4% to 18% for the 15-atm fill and from 3% to 15% for the 3-atm fill. A significant improvement in neutron yields indicates a better stability of the implosion shells when a picket was added to the drive laser pulse. A detailed analysis has revealed, however, that the radiation transport in CH shells leads to an additional shaping of the shell adiabat. The effect of such additional shaping will be addressed in future work.
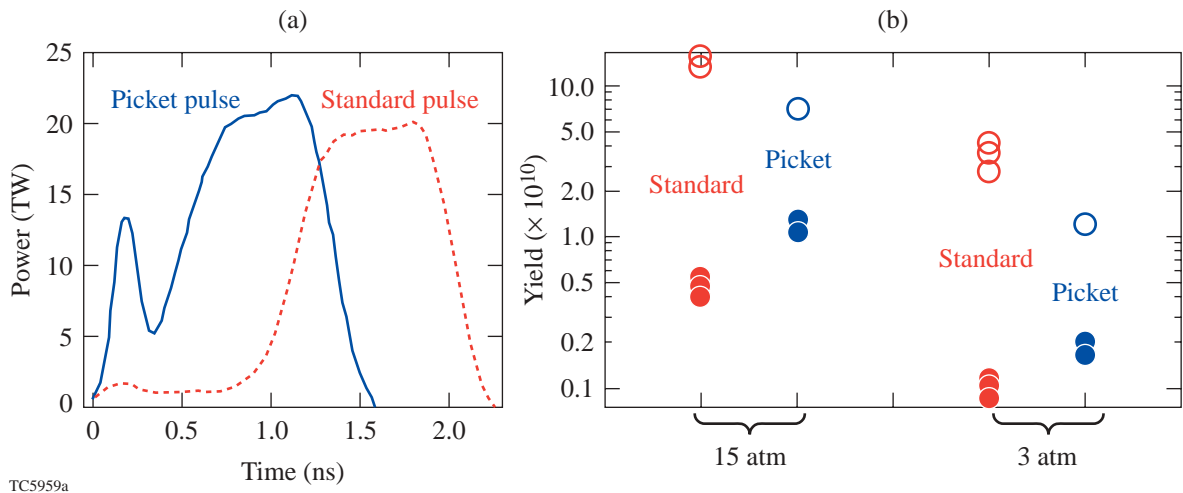

Figure 93.24
(a) Experimental laser pulses for the standard (dashed line) and picket (solid line) $\alpha = 2$, 33-μm-CH-shell target designs. (b) Neutron yield for the standard and picket pulses as predicted by the 1-D code *LILAC* (open circles) and obtained in the experiments (solid circles).

ACKNOWLEDGMENT

REFERENCES

1. J. D. Lindl, *Inertial Confinement Fusion: The Quest for Ignition and Energy Gain Using Indirect Drive* (Springer-Verlag, New York, 1998).

2. S. E. Bodner, D. G. Colombant, J. H. Gardner, R. H. Lehmberg, S. P. Obenschain, L. Phillips, A. J. Schmitt, J. D. Sethian, R. L. McCrory, W. Seka, C. P. Verdon, J. P. Knauer, B. B. Afeyan, and H. T. Powell, Phys. Plasmas **5**, 1901 (1998).

3. S. E. Bodner, Phys. Rev. Lett. **33**, 761 (1974); J. Sanz, Phys. Rev. Lett. **73**, 2700 (1994); V. N. Goncharov, R. Betti, R. L. McCrory, P. Sorotokin, and C. P. Verdon, Phys. Plasmas **3**, 1402 (1996); J. D. Kilkenny, S. G. Glendinning, S. W. Haan, B. A. Hammel, J. D. Lindl, D. Munro, B. A. Remington, S. V. Weber, J. P. Knauer, and C. P. Verdon, Phys. Plasmas **1**, 1379 (1994); S. G. Glendinning *et al.*, Phys. Plasmas **7**, 2033 (2000); C. Cherfils *et al.*, Phys. Rev. Lett. **83**, 5507 (1999); J. Grun *et al.*, Phys. Rev. Lett. **53**, 1352 (1984); J. P. Knauer, R. Betti, D. K. Bradley, T. R. Boehly, T. J. B. Collins, V. N. Goncharov, P. W. McKenty, D. D. Meyerhofer, V. A. Smalyuk, C. P. Verdon, S. G. Glendinning, D. H. Kalantar, and R. G. Watt, Phys. Plasmas **7**, 338 (2000).

4. S. Chandrasekhar, in *Hydrodynamic and Hydromagnetic Stability* (Oxford University Press, Glasgow, 1961).

5. S. E. Bodner, J. Fusion Energy **1**, 221 (1981).

6. J. D. Lindl and W. C. Mead, Phys. Rev. Lett. **34**, 1273 (1975).

7. L. D. Landau and E. M. Lifshitz, *Fluid Mechanics*, 2nd ed. (Butterworth-Heinemann, Newton, MA, 1987); D. L. Book and I. B. Bernstein, J. Plasma Phys. **23**, 521 (1980).

8. T. R. Boehly, D. L. Brown, R. S. Craxton, R. L. Keck, J. P. Knauer, J. H. Kelly, T. J. Kessler, S. A. Kumpan, S. J. Loucks, S. A. Letzring, F. J. Marshall, R. L. McCrory, S. F. B. Morse, W. Seka, J. M. Soures, and C. P. Verdon, Opt. Commun. **133**, 495 (1997).

9. J. Paisner *et al.*, Laser Focus World **30**, 75 (1994).

10. J. P. Knauer, V. N. Goncharov, P. W. McKenty, T. C. Sangster, R. Betti, V. Yu. Glebov, T. J. B. Collins, D. D. Meyerhofer, P. B. Radha, C. Stoeckl, J. A. Frenje, C. K. Li, R. D. Petrasso, and F. H. Séguin, "Improved Performance of Direct-Drive Implosions with a Laser-Shaped Adiabat," submitted to Physical Review Letters.

11. Ya. B. Zel'dovich and Yu. P. Raizer, *Physics of Shock Waves and High-Temperature Hydrodynamic Phenomena*, edited by W. D. Hayes and R. F. Probstein (Dover Publications, Mineola, NY, 2002).

12. R. J. Trainor and Y. T. Lee, Phys. Fluids **25**, 1898 (1982).

13. J. Delettrez and E. B. Goldman, Laboratory for Laser Energetics Report No. 36, University of Rochester (1976).

14. P. W. McKenty, V. N. Goncharov, R. P. J. Town, S. Skupsky, R. Betti, and R. L. McCrory, Phys. Plasmas **8**, 2315 (2001).

15. V. N. Goncharov, S. Skupsky, T. R. Boehly, J. P. Knauer, P. McKenty, V. A. Smalyuk, R. P. J. Town, O. V. Gotchev, R. Betti, and D. D. Meyerhofer, Phys. Plasmas **7**, 2062 (2000).

16. W. K. Levedahl and J. D. Lindl, Nucl. Fusion **37**, 165 (1997).

17. V. Lobatchev and R. Betti, Phys. Rev. Lett. **85**, 4522 (2000).

18. R. Betti, V. Lobatchev, and R. L. McCrory, Phys. Rev. Lett. **81**, 5560 (1998).

19. Laboratory for Laser Energetics LLE Review **79**, 121, NTIS document No. DOE/SF/19460-317 (1999). Copies may be obtained from the National Technical Information Service, Springfield, VA 22161.

20. R. Betti, V. N. Goncharov, R. L. McCrory, and C. P. Verdon, Phys. Plasmas **5**, 1446 (1998).

21. R. L. McCrory and C. P. Verdon, in *Computer Applications in Plasma Science and Engineering*, edited by A. T. Drobot (Springer-Verlag, New York, 1991), Chap. 11, pp. 291–325.

22. C. M. Bender and S. A. Orszag, *Advanced Mathematical Methods for Scientists and Engineers* (McGraw-Hill, New York, 1978).

23. R. Ishizaki and K. Nishihara, Phys. Rev. Lett. **78**, 1920 (1997).

24. V. N. Goncharov, Phys. Rev. Lett. **82**, 2091 (1999).

25. S. J. Han and B. R. Suydam, Phys. Rev. A **26**, 926 (1982); A. I. Kleev and A. L. Velikovich, Plasma Phys. Control. Fusion **32**, 763 (1990).

26. S. Skupsky, R. W. Short, T. Kessler, R. S. Craxton, S. Letzring, and J. M. Soures, J. Appl. Phys. **66**, 3456 (1989).

27. T. J. B. Collins and S. Skupsky, Phys. Plasmas **9**, 275 (2002).

28. V. N. Goncharov, P. McKenty, S. Skupsky, R. Betti, R. L. McCrory, and C. Cherfils-Clérouin, Phys. Plasmas **7**, 5118 (2000).